

# SPARC: Spine with Prismatic and Revolutive Compliance for Quadruped Robots

Yue Wang

School of Electronic and Computer Science (ECS)

University of Southampton

United Kingdom

Email: Yue.Wang@soton.ac.uk

**Abstract**—Quadruped mammals coordinate spinal bending and axial compression to enhance locomotion agility and efficiency. However, existing robotic spines typically lack the active compliance required to support such dynamic behaviours. We present SPARC, a compact 3-DoF sagittal-plane spine module that enables simultaneous revolute and prismatic motions within a 1.26 kg package. Using a floating-base impedance controller, we facilitate independent, task-space tuning of spinal stiffness and damping to mimic biological load-bearing strategies. Benchtop experiments confirm high-fidelity rendering of commanded impedance, with linear force-displacement error within 1.5%. Systematic locomotion simulations reveal a critical speed-dependency: while low-speed efficiency is insensitive to spinal properties, precise impedance tuning becomes indispensable for high-speed performance. Our results demonstrate that an optimally compliant spine reduces power consumption by 21% at 0.9 m/s compared to a rigid-spine baseline. This efficiency gain is mechanically attributed to the spine’s role in augmenting stride length and acting as a mechanical low-pass filter to attenuate high-frequency torque fluctuations. SPARC provides an open-source platform for systematic studies of spine compliance in legged locomotion. Available at: [github.com/YueWang996/sparc](https://github.com/YueWang996/sparc).

## I. INTRODUCTION

Quadruped mammals use flexible spines to lengthen stride, absorb landing impacts, and generate thrust, achieving agile and efficient motions beyond what rigid torsos can provide [2, 33]. Research indicates that quadruped animals actively modulate spinal kinematics across speeds to optimise locomotion, utilising spinal flexion to enhance stride length and elastic energy storage [26, 4]. Most robotic quadrupeds, however, employ rigid trunks to simplify structure and control [18, 17], limiting energy shaping and workspace modulation during high-speed manoeuvres.

Current robotic spine designs involve trade-offs between passive efficiency, active controllability, and continuous power modulation. *Passive compliant spines* provide efficient elastic energy storage but lack the actuation required for propulsive thrust, which restricts their utility to steady-state gaits [32]. Conversely, *actuated spines* using position control allow for precise trajectory tracking of the spine; however, the high stiffness inherent in these systems suppresses natural dynamics, leading to energy dissipation during impacts rather than recycling them [19]. While *spring-loaded mechanisms* can generate axial thrust, they often lack active retraction capabilities, restricting their application to discrete manoeuvres

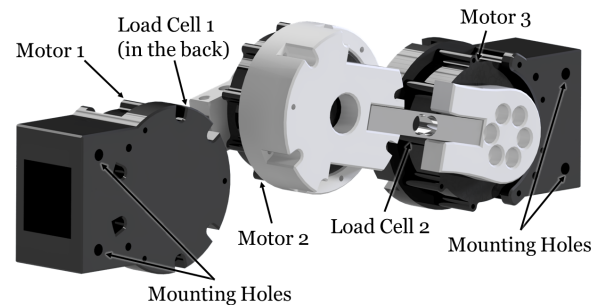
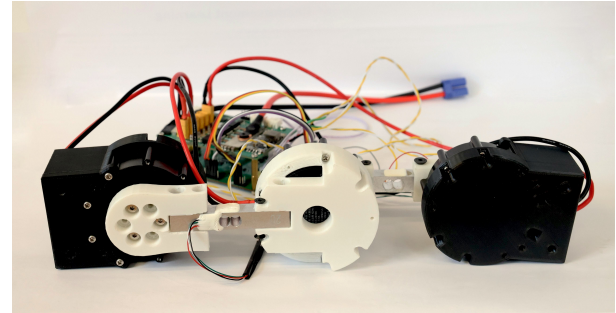


Fig. 1: The compact SPARC system. It is designed to mount between the fore and hind body segments of a quadruped robot. Top: assembled prototype used in experiments. Bottom: structure of the spine unit.

rather than periodic gait cycles [31]. These specialised designs contrast with mammalian anatomy, where articulated vertebrae coordinate bending and axial compression. This coordination enables animals to attenuate impacts and generate propulsion [3]. By not accounting for the role of axial load-bearing [27], existing robotic systems often lack the integrated regulation of stiffness and kinematics observed in biological locomotion.

To address this gap, we present **SPARC** (Spine with Prismatic And Revolutive Compliance, as shown in Fig. 1), a compact, open-source 3-DoF sagittal-plane spine module designed to actively regulate both bending and axial extension between fore and hind body segments. The main contributions of this paper are:

- 1) We develop a 1.26 kg self-contained spine module incorporating three quasi-direct-drive (QDD) actuators. The multi-link serial architecture enables both revolute bending and prismatic extension, simultaneously.
- 2) We implement a floating-base task-space impedance controller that facilitates axis-selective regulation of

stiffness and damping. This framework enables independent tuning of longitudinal and rotational compliance, capturing the functional versatility of biological spines.

- 3) We systematically investigate the impact of spine impedance on energetics, revealing that active compliance adjustment is indispensable for high-speed efficiency. Our analysis demonstrates a 21% reduction in power consumption compared to a rigid-spine baseline, mediated by stride length augmentation and mechanical filtering of torque chattering.

The remainder of this paper is organised as follows. Section II reviews related work. Section III details the SPARC hardware and control, followed by experiments in Section IV and conclusions in Section V.

## II. RELATED WORK

The advantages of spinal flexibility in quadrupeds, particularly the coupling of sagittal flexion and compression, are well-studied in [3, 2]. However, replicating these behaviours in legged robots requires addressing constraints in both mechanical design and compliance regulation.

### A. Robotic spine design

Most robotic spines focus on revolute motion. Early designs introduced sagittal bending to extend leg workspace [11] and improve efficiency [19, 8, 5, 9], while more recent works explore multi-axis coordination for turning agility and lateral manoeuvrability [20, 7, 6]. While these architectures provide clear kinematic benefits, active spinal actuation can increase energy consumption compared to rigid baselines if impedance is not optimised [15]. Furthermore, the absence of an axial degree of freedom prevents these systems from modulating body length or absorbing landing impacts through controlled compression, constraining their capacity for energy profiling.

Prismatic motion in robotic spines is primarily limited to passive or manually adjustable mechanisms. Ye et al. implemented a spring-loaded spine capable of impact absorption through manual pre-compression [31]. While effective for discrete manoeuvres like jumping, the requirement for manual resets precludes its use in continuous periodic gaits. Although simulation studies suggest that closed-loop axial compliance can enhance stability and acceleration [30, 14], experimental

hardware validation of continuously controllable prismatic motion remains absent from the literature.

### B. Realisation of Compliance

Compliance realisation significantly dictates a robot’s functional adaptability. Early designs utilised passive materials for energy storage [32], but their static mechanical properties preclude task-specific tuning. Mechanically variable stiffness (MVS) mechanisms introduced adjustability via hardware parameter changes [12, 8, 24], though often at the cost of increased mechanical complexity and low control bandwidth.

### C. Realization of Compliance

Compliance realisation significantly dictates a robot’s functional adaptability. Early designs utilised passive materials for energy storage [32], but their static mechanical properties preclude task-specific tuning. Mechanically variable stiffness (MVS) mechanisms introduced adjustability via hardware parameter changes [12, 8, 24], though often at the cost of increased mechanical complexity and low control bandwidth.

Quasi-direct-drive (QDD) actuators enable a software-defined paradigm: high-bandwidth impedance tuning via joint-level torque control [10, 21]. However, independent joint-space regulation leads to coupled task-space compliance, where Cartesian stiffness becomes a configuration-dependent function of the kinematic structure. This prevents the explicit shaping of anisotropic compliance, such as the decoupled vertical support and horizontal flexibility observed in biological spines [3]. Achieving such axis-selective behaviour requires task-space impedance control to map desired Cartesian stiffness (along  $x, z, \theta$ ) to joint torques via the system Jacobian. As summarised in Table I, SPARC fills this gap by integrating simultaneous revolute and prismatic motion with real-time, axis-selective impedance, providing a unified platform for continuous closed-loop control of spinal compliance.

## III. METHODOLOGY

To replicate the functional versatility of mammalian spines, the robotic mechanism must support coordinated axial compression and sagittal bending. We address this through the SPARC module, which utilises a multi-link serial chain to render tunable task-space impedance. As illustrated in Fig. 2,

TABLE I: Comparison of spine designs in quadruped robots. SPARC is the first to combine revolute and prismatic motion with real-time tunable, axis-selective compliance under continuous closed-loop control.

Work	Revolute Motion	Prismatic Motion	Control Type	Real-time Tunable	Axis-selective Compliance	Key Capability
Lynx [12]	✓	✗	Passive	✗	✗	Gait modulation
Bobcat [19]	✓	✗	Position Control	✗	✗	Modest efficiency gains
INU Robot [11]	✓	✗	Reactive Control	✗	✗	Extended workspace
Yat-sen Lion [20]	✓	✗	Model Predictive Control	✗	✗	Load distribution
Planar Robot[8]	✓	✗	Stiffness Regulation	✓	✗	Adjustable compliance
Twisting Spine [7]	✓	✗	Trajectory Optimization	✗	✗	Turning agility
SCIQ [31]	✗	✓	Discrete Switching	✗	✗	Impact absorption
Prismatic Spine Robot [14]	✗	✓	Trajectory Optimization	—	—	Acceleration study
Prismatic Spine Robot [30]	✗	✓	Trajectory Optimization	—	—	Long jump performance
<b>SPARC (this work)</b>	✓	✓	<b>Impedance Control</b>	✓	✓	<b>Tunable anisotropic compliance</b>

the system integrates a high-bandwidth impedance controller with a standard bounding gait scheduler. This section details the hardware realisation, the derivation of the task-space control laws, and the real-time embedded implementation.

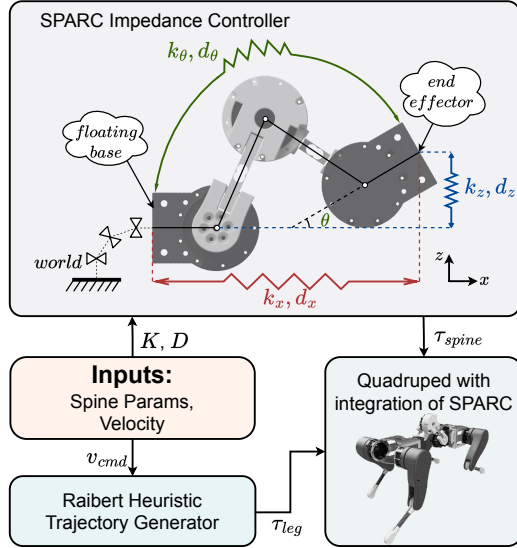


Fig. 2: System integration of SPARC. The impedance controller regulates task-space compliance ( $K, D$ ), while a Raibert-based heuristic generates bounding trajectories for the quadruped testbed.

### A. Hardware Design

SPARC is a self-contained module comprising a 3-DoF active spine, a Motion Control Board (MCB), and a Power Management Unit (PMU). The module provides sagittal-plane motion via three Xiaomi Cybergear QDD actuators, each capable of 12 N·m peak torque. To preserve the high back-drivability and transparency inherent in the QDD actuators, the spine links are 3D-printed to be lightweight, with 75% of the total 1.26 kg mass concentrated near the joint axes. This mass distribution minimises link inertia, allowing the actuators to respond rapidly to interaction forces and facilitating high-bandwidth task-space control.

For state estimation, an onboard 6-axis IMU provides real-time attitude measurement, enabling the world-to-body transformation required for floating-base spine impedance control. This ensures the spine maintains consistent task-space restorative forces regardless of the robot’s base orientation. While the control loop utilises high-resolution actuator encoders, two load cells are integrated into the central links to provide independent, ground-truth torque measurements. These sensors are essential for experimental validation, as they provide a physical force reference that avoids the potential bias and circularity of relying solely on internal current-based torque estimation.

The SPARC module is designed for integration into a custom 8-DoF quadrupedal platform, serving as the compliant link between the fore and hind body segments. To evaluate the impact of spinal impedance on locomotion, we utilise

a high-fidelity simulation model of the full-body system. Locomotion is governed by a bounding gait scheduler that generates leg trajectories, which are tracked by a PD controller with gain-scheduling based on the natural frequency of the swing dynamics [10]. This integrated framework allows for a systematic study of how varying spine parameters (specifically stiffness and damping) interact with gait settings across diverse locomotion tasks.

### B. Impedance Control of SPARC

We developed a model-based impedance controller to command the spine as a compliant, spring-like mechanism. We model SPARC as part of a floating-base system operating in the sagittal plane. As shown in Fig. 2, the task-space state  $x = [x, z, \theta]^T \in \mathbb{R}^3$  represents the end-effector pose (horizontal position, vertical position, pitch angle). While the kinematics are defined relative to the base link, the task-space compliance is aligned with the global gravity vector using the IMU-derived orientation. The full system has generalized coordinates  $q \in \mathbb{R}^{10}$  (7 for floating base  $q_{\text{base}}$  including position and unit quaternion orientation, and 3 for spine actuators  $q_s$ ) and velocities  $v \in \mathbb{R}^9$  (6 for base spatial velocity, 3 for spine joint velocities  $v_s$ ).

The dynamics of the floating-base system can be described by the standard formulation [13]:

$$M(q)\dot{v} + h(q, v) = \tau + J^T F_{\text{ext}}, \quad (1)$$

where  $M(q) \in \mathbb{R}^{9 \times 9}$  is the mass matrix,  $h(q, v) = C(q, v) + g(q)$  collects Coriolis and gravity effects, and  $\tau \in \mathbb{R}^9$  are the generalized torques acting in direction of generalized coordinates. Rather than deriving these terms analytically, we compute  $M(q)$  and  $h(q, v)$  using the Composite Rigid Body Algorithm (CRBA) and the Recursive Newton–Euler Algorithm (RNEA), respectively [13].

The full system mass matrix  $M(q)$  is divided into blocks corresponding to base and spine coordinates:

$$M(q) = \begin{bmatrix} M_{bb}(q) & M_{bs}(q) \\ M_{sb}(q) & M_{ss}(q) \end{bmatrix}, \quad (2)$$

where  $M_{bb} \in \mathbb{R}^{6 \times 6}$  is the base inertia,  $M_{ss} \in \mathbb{R}^{3 \times 3}$  is the spine inertia, and  $M_{sb} = M_{bs}^T \in \mathbb{R}^{3 \times 6}$  captures inertial coupling between base and spine motion. Similarly, we partition the nonlinear vector  $h = [h_b^T, h_s^T]^T$ , the generalized forces  $\tau = [\tau_b^T, \tau_s^T]^T$ , and the Jacobian  $J = [J_b, J_s]$ .

Extracting the equations corresponding to the spine dynamics yields:

$$M_{sb}(q)\dot{v}_{\text{base}} + M_{ss}(q)\dot{v}_s + h_s(q, v) = \tau_s + J_s^T F_{\text{ext}}. \quad (3)$$

Although Eq. (3) represents the complete dynamics, we omit the coupling term  $M_{sb}(q)\dot{v}_{\text{base}}$  to enhance the spine’s reactive transparency. In a physical mass-spring system, base acceleration naturally causes the suspended mass to lag due to inertia. Actively compensating for this coupling would force the actuators to cancel this inherent lag, potentially leading to excessive stiffness during rapid manoeuvres. By dropping this

term, we allow the spine to respond naturally to inertial loads during impact events. Consequently, the dynamics simplify to:

$$M_{ss}(q)\dot{v}_s + h_s(q, v) = \tau_s + J_s^\top F_{\text{ext}}, \quad (4)$$

For the computation of  $h_s(q, v)$ , we use the full state vector  $q$  where the IMU provides the real-time base orientation. This ensures exact gravity compensation in the local frame. As a result, the impedance behaviour aligns with the robot's body axes regardless of terrain slope.

The desired compliant behaviour is synthesized by imposing the dynamics of a virtual mass–spring–damper system in task space:

$$\Lambda(x)\ddot{\tilde{x}} + D\dot{\tilde{x}} + K\tilde{x} = -F_{\text{ext}}, \quad (5)$$

where  $\tilde{x} = x_d - x$  is the task-space tracking error. The operational space inertia matrix is computed as  $\Lambda(x) = (J_s M_{ss}^{-1} J_s^\top)^{-1}$ . To allow for independent impedance regulation across the different degrees of freedom, we employ diagonal stiffness and damping matrices:

$$K = \text{diag}(k_x, k_z, k_\theta), \quad D = \text{diag}(d_x, d_z, d_\theta), \quad (6)$$

corresponding to the horizontal, vertical, and pitch axes, respectively.

Based on this target model, the impedance control law is formulated as:

$$\begin{aligned} F_{\text{imp}} &= K\tilde{x} + D\dot{\tilde{x}}, \\ F_{\text{comp}} &= \Lambda(x)\dot{J}_s(q, v)v_s, \\ \tau_s &= h_s(q, v) + J_s^\top(q)(F_{\text{imp}} - F_{\text{comp}}). \end{aligned} \quad (7)$$

Here,  $F_{\text{imp}}$  provides the restorative stiffness and damping forces, while  $F_{\text{comp}}$  cancels the task-space Coriolis and centrifugal bias. As before,  $h_s$  compensates for joint-space gravitational and nonlinear effects. It is straightforward to verify that substituting (7) into the spine dynamics (3) and projecting into task space yields the target system in (5).

The operational space inertia matrix  $\Lambda(x) = (J_s M_{ss}^{-1} J_s^\top)^{-1}$  is computed using a damped least-squares formulation [23] to ensure numerical robustness.

Notably, our controller preserves the intrinsic system inertia  $\Lambda(x)$ , rather than shaping it to a desired diagonal inertia. While active inertia shaping can decouple the task axes, it requires high-fidelity force sensing at the end effector [1], which is impractical for the compact SPARC module. Consequently, minor inertial coupling remains. However, given the lightweight design of the spine mechanism, these inertial effects are negligible compared to the dominant compliant forces produced by the diagonal stiffness and damping matrices,  $K$  and  $D$ .

### C. Friction Compensation

Since joint friction limits torque fidelity on real hardware, we compensate for these effects using a smooth Stribeck model [22] applied element-wise to each joint:

$$\tau_{f,i} = \left[ \tau_{c,i} + (\tau_{s,i} - \tau_{c,i})e^{-(|v_{s,i}|/v_{st})^\delta} \right] \tanh(\beta v_{s,i}) + b_i v_{s,i}, \quad (8)$$

where  $\tau_{c,i}$ ,  $\tau_{s,i}$ , and  $b_i$  denote the Coulomb friction, static friction, and viscous coefficient for the  $i$ -th joint, respectively. The parameter  $v_{st}$  is the Stribeck velocity threshold, while  $\delta$  and  $\beta$  are shape parameters governing the transition smoothness. This formulation ensures a smooth transition between static and Coulomb friction, minimising chattering near zero velocity while accounting for the nonlinearities observed in QDD actuators. Finally, the total control input sent to the spine actuators is the sum of the impedance and friction compensation torques:

$$\tau_{\text{cmd}} = \tau_s + \tau_f. \quad (9)$$

### D. Software and Real-Time Implementation

The control framework is implemented in C. To ensure deterministic execution under hard real-time constraints, the control loop is managed by FreeRTOS as a high-priority, preemptive task running at 1 kHz. In each control cycle, the system first updates the kinematic chain and the task-space Jacobian  $J_s$ . Subsequently, the full-system mass matrix  $M(q)$  and nonlinear terms  $h(q, v)$  are evaluated via our custom, optimised implementations of the CRBA and RNEA algorithms, respectively. Finally, the impedance control law (Eq. (7)), incorporating the friction compensation term (Eq. (8)), is computed to generate torque commands which are transmitted to the actuators.

To handle the computational load efficiently, we leverage the ARM CMSIS-DSP library for dense matrix operations, particularly the matrix inversions required for the operational space inertia  $\Lambda(x)$ . With these optimisations, the entire control pipeline completes in approximately 290  $\mu\text{s}$ , providing a 70% timing margin within the 1 ms control period. This ensures high-frequency impedance tracking and system stability during high-speed locomotion.

## IV. EXPERIMENTS AND ANALYSIS

To validate the efficacy of the SPARC system, we conducted a two-phase experiment comprising benchtop characterisation and full-body locomotion simulation. First, hardware experiments on the isolated spine module were performed to verify the stiffness rendering and dynamic tracking performance via quasi-static loading and step-response tests. The experimental testbed is shown in Fig. 3. The detailed physical specifications of the spine links are summarised in Table II. Subsequently, to evaluate the locomotion performance, the spine unit was integrated into a quadruped robot model in the MuJoCo simulator [28] to investigate the necessity of impedance adaptation across varying locomotion speeds.

TABLE II: Physical parameters of the spine unit.

Spine Link Parameters			
Link	Mass (kg)	Length (mm)	$I_{xx}, I_{yy}, I_{zz}$ (kg·mm <sup>2</sup> )
Hind spine	0.377	63.2	181, 328, 228
Hind-mid spine	0.376	117.5	148, 502, 426
Front-mid spine	0.414	117.5	991, 175, 990
Front spine	0.060	63.2	44, 92, 61

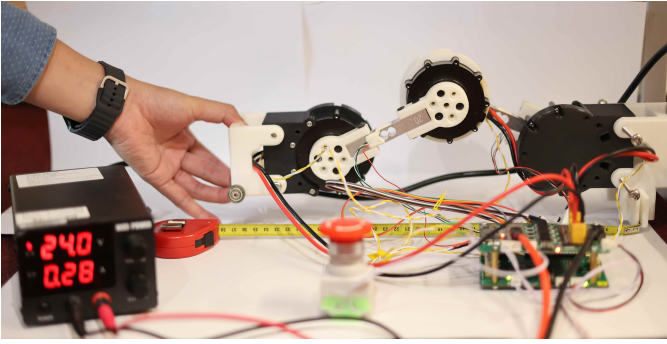


Fig. 3: Testbed for the SPARC spine unit. The base is fixed, while the end-effector is mechanically supported yet unconstrained along the  $x$ -axis to minimise friction. A horizontal force  $F_x$  is applied manually for quasi-static tests. The ruler provides a visual reference, while the precise displacement used for analysis is computed via encoder-based forward kinematics.

### A. Validation of Stiffness Rendering

The accuracy of the commanded horizontal stiffness  $k_x$  was evaluated via quasi-static push-pull tests. The spine end-effector was manually displaced along the  $x$ -axis while a load cell measured the restorative force  $F_x$ . For each commanded stiffness  $k_d \in \{300, 400, 500, 600, 700\}$  N/m, we conducted 10 continuous push-pull cycles. The corresponding displacement was computed from joint encoder measurements via forward kinematics.

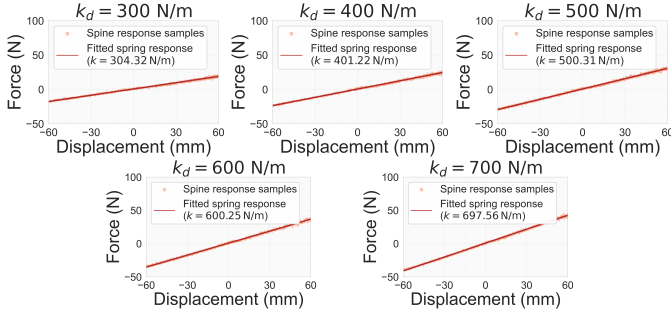


Fig. 4: Static force-displacement response for commanded  $k_x \in \{300, 400, 500, 600, 700\}$  N/m. Dots show measured data; solid lines show linear fits.

Figure 4 shows the force-displacement responses across all tested stiffness settings. The measured data exhibit highly linear behaviour with  $R^2 \geq 0.992$  for all cases. The fitted stiffness values match the commanded targets with a relative error of less than 1.5%, demonstrating high stiffness rendering fidelity. The system maintains linearity across the full displacement range ( $\pm 60$  mm), validating the efficacy of the impedance control law (7).

### B. Dynamical Damping Behaviour

To characterise the dynamic damping behaviour, we evaluated the step response of the spine’s end-effector in both simulation and physical experiments.

First, we conducted a simulation study in MuJoCo using the BARD solver [29] for controller implementation. To isolate the

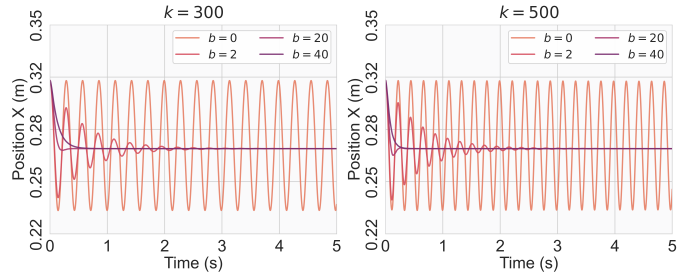


Fig. 5: Step response along  $x$ -axis of SPARC in simulation.

$x$ -axis dynamics, we constrained the motion along the  $z$ - and  $\theta$ -axes by setting high stiffness gains ( $[k_z, k_\theta] = [8000, 5]$ ) and damping coefficients ( $[d_z, d_\theta] = [5, 0.1]$ ). The end-effector was initialised at  $x = 0.315$  m, with the equilibrium position set to 0.273 m. We tested two stiffness values ( $k_x \in \{300, 500\}$  N/m) across four damping coefficients ( $d_x \in \{0, 2, 20, 40\}$  N·s/m). As depicted in Fig. 5, sustained oscillation is observed in the undamped case ( $d_x = 0$ ). As the damping coefficient increases from 2 to 40 N·s/m, the system behaviour shifts from underdamped to overdamped. Additionally, consistent with second-order system theory, the natural frequency increases with higher stiffness.

Following the simulation analysis, we replicated the step response experiments on the physical hardware to verify the controller’s performance under real-world conditions. The end-effector was manually displaced to an initial offset of 37 mm and released to oscillate freely. The resulting position trajectory was recorded as the system returned to equilibrium. The stiffness and damping parameters were identical to those used in the simulation, and each configuration was repeated 10 times to ensure statistical reliability.

Figure 6 presents the measured response (solid line with shaded  $\pm 1\sigma$  region) overlaid with the ideal mass-spring-damper behaviour (dashed line). In the physical system governed by Eq. (5), the operational space inertia  $\Lambda(x)$  varies continuously with the spine’s configuration. To facilitate comparison with an ideal linear second-order model (which assumes a constant mass), we identified the effective mass by fitting the theoretical response to the actual position trajectories, fixing stiffness and damping to their commanded values. The identified effective masses exhibited negligible variation across trials, justifying the use of a single constant mass for the ideal benchmark shown in the figure.

At higher damping values ( $d_x \in \{20, 40\}$  N·s/m), the measured response demonstrates excellent tracking fidelity, closely matching the ideal model across all trials. This confirms that, with sufficient damping, the controller accurately realises the desired task-space impedance and robustly enforces the target dynamics.

In the undamped case ( $d_x = 0$ ), where the feedforward term (Eq. (8)) is solely responsible for compensating physical joint friction, distinct deviations are observed. An accumulating phase lag emerges due to the frequency mismatch between the variable physical inertia  $\Lambda(x)$  and the constant effective mass

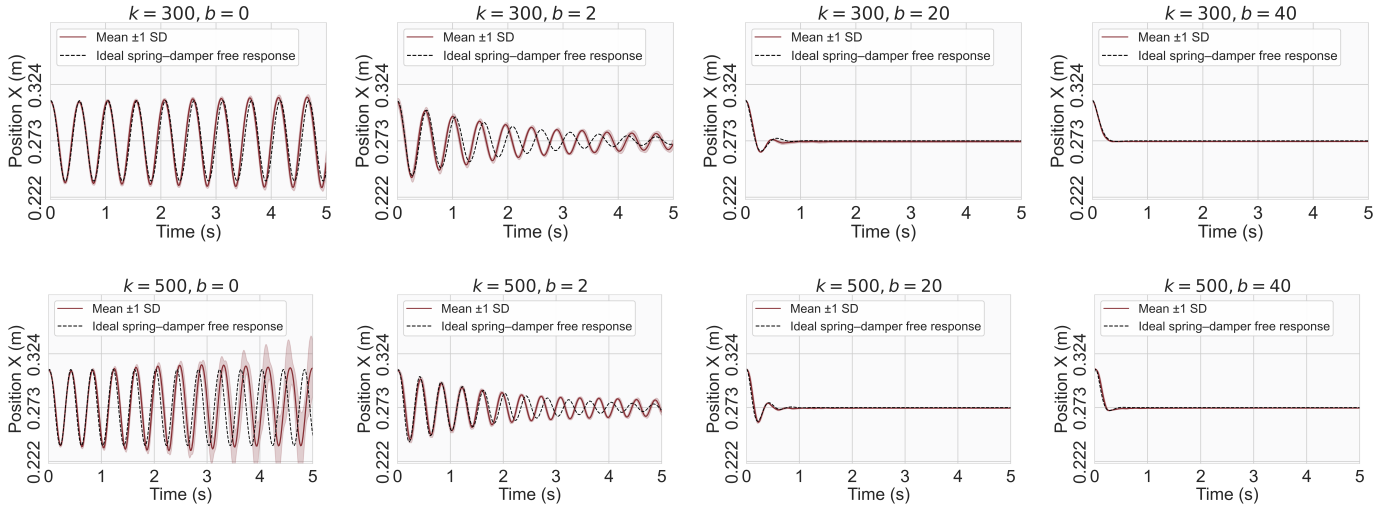


Fig. 6: Experimental validation of the variable impedance controller. The plots display the step response for two stiffness values ( $k_x \in \{300, 500\}$  N/m) under four distinct damping coefficients ( $d_x \in \{0, 2, 20, 40\}$  N·s/m). The measured response (solid line, mean  $\pm 1\sigma$  over 10 trials) is compared against the ideal mass-spring-damper system dynamics (dashed line).

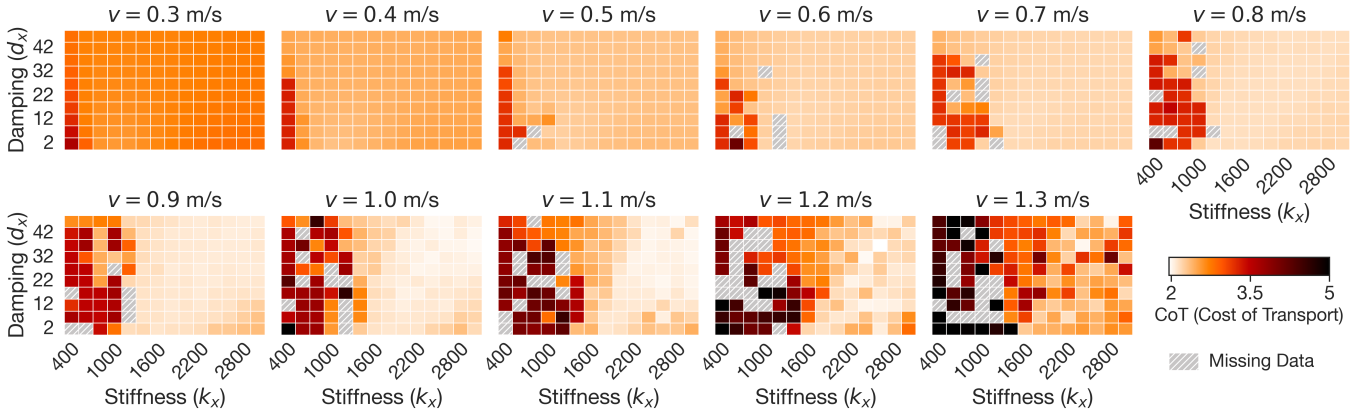


Fig. 7: Grid search results showing the relationship between spine impedance parameters and Cost of Transport (CoT) across velocity commands from 0.3 m/s to 1.3 m/s. Lighter colours indicate more efficient locomotion (lower CoT), while grey cells represent missing data where no stable gait was generated. The efficient parameter region (light colour) shrinks as speed increases, indicating that precise tuning of spine stiffness and damping becomes increasingly critical for energy efficiency at higher velocities.

of the ideal model. Furthermore, the variance of the measured response (indicated by the widening shaded region) increases over time. This effect is more pronounced at higher stiffness ( $k = 500$  N/m), where larger restorative forces amplify the impact of friction compensation errors. This amplitude instability arises because, in the absence of active damping, the system lacks the mechanism to dissipate the energy introduced by friction modelling inaccuracies. Consequently, slight over- or under-compensation leads to slowly growing or decaying oscillations.

At low damping ( $d_x = 2$  N·s/m), the response gradually develops a phase lead relative to the ideal model as oscillations decay. This behaviour arises from the dominance of Stribeck friction effects at low velocities. As the oscillation amplitude decreases, joint velocities drop into the nonlinear Stribeck region, governed by the velocity threshold  $v_{st}$  and shape factor  $\delta$  in Eq. (8). Since these secondary parameters are difficult to

characterise precisely, a slight over-estimation of the friction magnitude produces an excessive feedforward torque. This torque accelerates the system’s return to equilibrium, effectively increasing the oscillation frequency. Despite these minor low-speed artefacts, the overall results validate the controller’s design, with higher commanded damping consistently reducing overshoot and settling time.

### C. Parametric Sensitivity of Locomotion Efficiency

Since the SPARC mechanism provides tunable stiffness and damping capabilities, it allows us to investigate the effects of spine impedance on locomotion speed and energy efficiency. We conducted MuJoCo simulations of the SPARC-integrated quadruped robot, as shown in Fig. 2. The robot was configured to execute a bounding gait. The swing phase trajectory is determined by the Raibert heuristic [25], while propulsion during the stance phase is governed by a ground reaction force controller to track velocity commands. The computed forces

are then mapped to leg joint torques using the leg Jacobians [10].

In the simulation, we performed a grid search over stiffness  $k_x \in [400, 3000]$  N/m and damping  $d_x \in [2, 47]$  N·s/m to identify parameter combinations that minimise the Cost of Transport\* (CoT) across commanded forward velocities ranging from 0.3 m/s to 1.3 m/s (0.1 m/s resolution). Fig. 7 depicts the results. Each cell represents the CoT for a specific stiffness-damping pair, where lighter colours indicate lower CoT (higher efficiency).

At low speeds (e.g.,  $v_{cmd} = 0.3$  m/s), the CoT is relatively insensitive to spine parameters, and the locomotion is generally inefficient regardless of the parameter combination selected. However, as the speed increases to the medium range (0.4–0.8 m/s), optimal performance generally requires stiffer configurations ( $k_x > 1600$  N/m), while damping variations have a negligible impact on the CoT. At high speeds (1.0–1.3 m/s), the efficient regions (light colours) become increasingly concentrated, indicating high sensitivity to spine parameters. Inappropriate configurations often fail to generate stable locomotion, and specific tuning becomes critical for efficiency (e.g.,  $k_x = 2600$  N/m and  $d_x = 32$  N·s/m at  $v_{cmd} = 1.3$  m/s). These results demonstrate that while the bounding gait is well-suited for high-speed locomotion, the tunable stiffness and damping of the spine are critical from an efficiency perspective. This finding aligns with the gait transition mechanisms observed in quadruped animals [16].

#### D. Analysis of Energy Efficiency

To quantify the energy efficiency, we measured the average power consumption across different command speeds for both the compliant and rigid configurations<sup>†</sup>. The reported power consumption is defined as the time-average power<sup>‡</sup> of all active joints. To ensure the validity of the comparison, we applied a velocity tracking filter to the experimental data. Only trials where the actual forward velocity remained within a 30% tolerance of the commanded velocity (i.e.  $|v_{actual} - v_{cmd}|/v_{cmd} \leq 0.3$ ) were retained. For the compliant spine configuration, the *Optimal* and *Worst* data points correspond to the trials yielding the minimum and maximum CoT, respectively, within this valid set. The *Average* curve denotes the mean of all valid trials. For the rigid-spine robot baseline, the heuristic gait controller exhibited higher velocity variance; thus, the same 30% tracking filter was strictly applied to exclude unstable runs and ensure that the reported power consumption reflects valid locomotion states. The curves in Fig. 8 are fitted to these validated data points.

For the compliant spine robot, power consumption is relatively insensitive to parameter variations at low to medium speeds ( $v \leq 0.7$  m/s). In this region, the average consumption

\*Defined as  $CoT = P_{avg}/(mgv_{avg})$ , where  $P_{avg}$  is the mean of the sum of absolute mechanical power across all joints,  $m$  is the total mass of the robot,  $g$  is gravitational acceleration, and  $v_{avg}$  is the average forward velocity.

<sup>†</sup>The Raibert heuristic parameters are exactly the same.

<sup>‡</sup>The power is calculated as  $\bar{P} = (1/T) \sum_{t=0}^T \sum_i |\tau_i(t) \dot{q}_i(t)|$ , where  $T$  is the duration of the valid trial (5 s in our simulation), and  $\tau_i(t)$ ,  $\dot{q}_i(t)$  represent the instantaneous torque and velocity of the  $i$ -th joint, respectively.

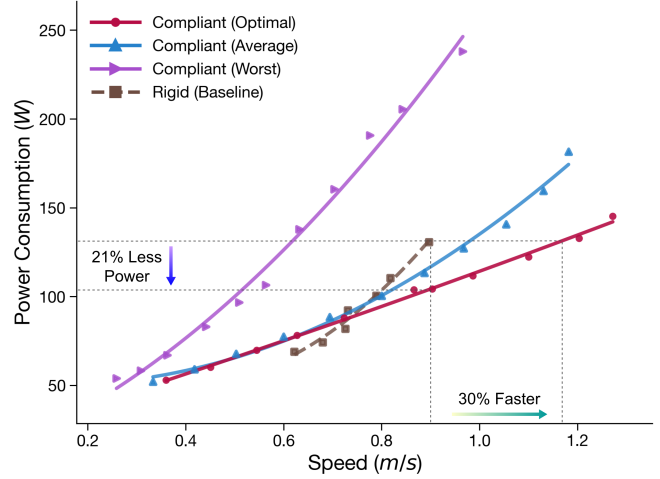


Fig. 8: Power consumption vs. speed. The curves show the optimal, average, and worst-case performance of the compliant robot compared to the rigid baseline. Data points represent valid trials with a velocity tracking error of less than 30%.

tracks closely with the optimal curve, consistent with the broad effective parameter space observed in Fig. 7. However, a significant divergence occurs at higher velocities ( $v > 0.7$  m/s), where the worst-case power consumption escalates to more than double that of the optimal setting. This sharp contrast demonstrates that while the robot is tolerant to parameter mismatch at low speeds, precise impedance tuning is indispensable for energy efficiency during high-speed locomotion.

Comparing the compliant spine configuration against the rigid baseline reveals a distinct crossover in performance. At lower bounding speeds ( $v_{cmd} < 0.7$  m/s), the rigid-spine robot consumes less power. This is likely because the rigid connection passively maintains the relative posture of the front and hind bodies, whereas the compliant spine requires active motor torque to maintain this posture, consuming power without contributing to forward velocity. However, as the speed demand increases, the compliant spine demonstrates superior efficiency. At 0.9 m/s, using the optimal spine parameters reduces power consumption by 21% compared to the rigid baseline. Additionally, given a fixed power budget (e.g.,  $\sim 130$  W), the compliant configuration achieves locomotion speeds up to 30% faster than its rigid configuration (1.17 m/s vs. 0.90 m/s). These results confirm that an optimally tuned compliant spine is not merely a passive structure but a critical factor for efficient high-speed locomotion.

#### E. Mechanism of Efficiency Enhancement

To elucidate the physical principles underlying the efficiency gains, we analysed the instantaneous power dynamics and the spectral characteristics of the joint torques.

The core mechanism of the efficiency enhancement at high speeds is revealed in the spine dynamics shown in Fig. 9 (Bottom). At the start of each gait cycle (hind leg propulsion), the spine begins to extend from a pre-compressed state. Notably, this extension phase corresponds to negative work

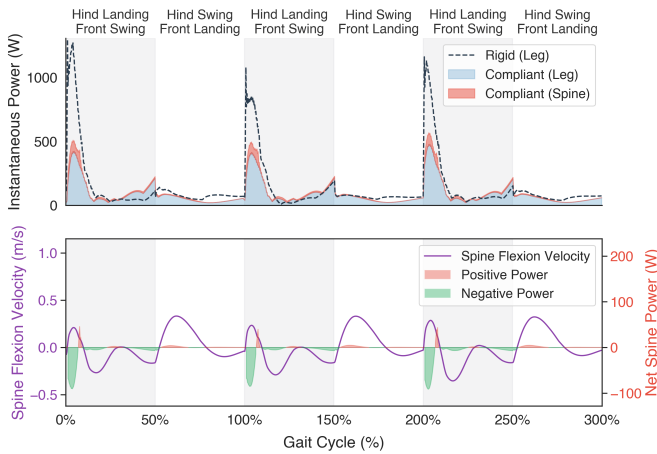


Fig. 9: Temporal analysis of power consumption and spine dynamics over three full gait cycles at 0.9 m/s. **Top:** Instantaneous power consumption. The dashed line represents the aggregated power of the eight leg joints in the rigid-spine robot baseline. The stacked shaded areas show the compliant robot’s power, divided into leg joints (blue) and spine joints (red). Note that the compliant configuration significantly reduces the peak power demand of the legs during the propulsion phases. **Bottom:** Spine flexion velocity and net mechanical power. The red shaded regions indicate positive power where the spine actively extends to assist motion, while the green shaded regions show negative power where the spine is passively moved, acting as a damper to dissipate vibration.

(green regions), indicating that the spine’s impedance acts as a damper, effectively absorbing the energy spikes generated by the kick-off. Subsequently, the spine transitions to a phase of positive work (red regions), actively extending to propel the front body forward. As the front legs land and the hind legs swing forward, the reaction moment induces further extension, followed by a compression phase driven by the inherent inertia of the posterior body, which resets the mechanism for the next cycle.

This dynamical energy exchange improves efficiency through two coupled effects. Primarily, the active flexion-extension cycle significantly augments the stride length, allowing the robot to cover more distance per energetic cost. Secondly, as reflected by the frequency domain analysis in Fig. 10 (Right), the spine acts as a mechanical low-pass filter at high speeds ( $v = 0.90$  m/s). It preserves the fundamental gait frequency while attenuating high-frequency torque chattering ( $> 30$  Hz). This confirms that the spine smooths the actuation profile by shaving off sharp impact peaks, preventing the leg actuators from operating in inefficient high-torque regions.

In contrast, this synergy is absent at lower speeds (e.g.  $v = 0.62$  m/s). In this region, the gait does not require significant stride augmentation from the spine. Consequently, instead of smoothing the motion, the compliant spine introduces instability. As shown in Fig. 10 (Left), it amplifies vibrations across the broad frequency spectrum (red area). Without the kinematic benefit of stride lengthening to offset these parasitic oscillations, the compliant robot consumes more power than its rigid counterpart. Thus, the spine is beneficial only when its dynamics are synchronised with the high-speed locomotion rhythm to harness the inertial energy exchange.

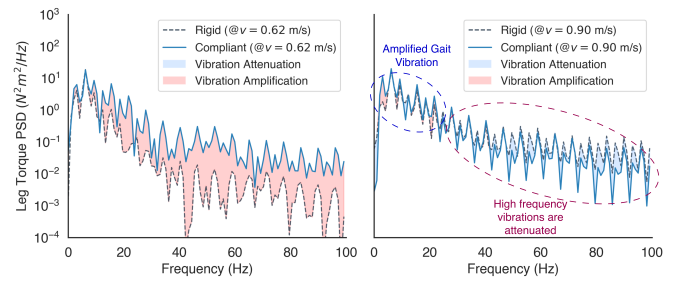


Fig. 10: Power Spectral Density (PSD) of leg joint torque for rigid and compliant configurations. **Left:** At low speed ( $v = 0.62$  m/s), the compliant spine exhibits broad vibration amplification (red area) across the frequency spectrum. **Right:** At high speed ( $v = 0.90$  m/s), the compliant spine acts as a mechanical low-pass filter. It attenuates high-frequency vibrations ( $> 30$  Hz, purple dashed circle) while maintaining the fundamental gait frequency, thereby reducing energy wastage from torque chattering.

## V. CONCLUSIONS

We have presented SPARC, a validated, open-source platform for investigating 3-DoF sagittal spine compliance in quadrupedal robots. Benchtop experiments confirm that our floating-base impedance controller accurately regulates stiffness and damping in task space, establishing a reliable basis for dynamic locomotion studies. Crucially, our systematic investigation using this platform reveals that the benefits of spinal compliance are highly speed-dependent: while low-speed locomotion is relatively insensitive to parameter changes, high-speed efficiency relies heavily on precise impedance tuning. We demonstrate that an optimal compliant configuration yields a 21% reduction in power consumption compared to a rigid spine, attributed to stride length augmentation and the mechanical filtering of high-frequency torque chattering. This study provides design references for compliant quadrupedal robots and offers a robotic perspective on the mechanics of locomotion efficiency.

Future work will address two main issues. First, we plan to validate the predicted energy savings on a complete physical quadruped. Second, we aim to improve control robustness. Currently, unmodelled friction makes the system sensitive at near-zero damping levels. To overcome this and the complexity of manual tuning, we will develop a data-driven framework to dynamically adapt stiffness and damping parameters in real-time, ensuring stable and efficient locomotion in practical applications.

## REFERENCES

- [1] Alin Albu-Schaffer, Christian Ott, Udo Frese, and Gerd Hirzinger. Cartesian impedance control of redundant robots: Recent results with the dlr-light-weight-arms. In *2003 IEEE International conference on robotics and automation (Cat. No. 03CH37422)*, volume 3, pages 3704–3709. IEEE, 2003.
- [2] R McN Alexander, Nicola J Dimery, and RF Ker. Elastic structures in the back and their role in galloping in some mammals. *Journal of zoology*, 207(4):467–482, 1985.
- [3] Bonnie V Beaver. *Canine behavior: a guide for veterinarians*. 1999.

- [4] John EA Bertram and Anne Gutmann. Motions of the running horse and cheetah revisited: fundamental mechanics of the transverse and rotary gallop. *Journal of the Royal Society Interface*, 6(35):549, 2008.
- [5] Shounak Bhattacharya, Abhik Singla, Dhaivat Dhokakiya, Shalabh Bhatnagar, Bharadwaj Amrutur, Ashitava Ghosal, Shishir Kolathaya, et al. Learning active spine behaviors for dynamic and efficient locomotion in quadruped robots. In *2019 28th IEEE International conference on robot and human interactive communication (RO-MAN)*, pages 1–6. IEEE, 2019.
- [6] Zhenshan Bing, Alex Rohregger, Florian Walter, Yuhong Huang, Peer Lucas, Fabrice O Morin, Kai Huang, and Alois Knoll. Lateral flexion of a compliant spine improves motor performance in a bioinspired mouse robot. *Science Robotics*, 8(85):eadg7165, 2023.
- [7] J Caporale, Zeyuan Feng, Shane Rozen-Levy, Aja Mia Carter, and Daniel E Koditschek. Twisting spine or rigid torso: Exploring quadrupedal morphology via trajectory optimization. In *2023 IEEE International Conference on Robotics and Automation*, number 886, 2023.
- [8] Dongliang Chen, Ningjie Li, Hong Wang, and Lei Chen. Effect of flexible spine motion on energy efficiency in quadruped running. *Journal of Bionic Engineering*, 14(4):716–725, 2017.
- [9] Utku Culha. An actuated flexible spinal mechanism for a bounding quadrupedal robot. Master’s thesis, Bilkent Universitesi (Turkey), 2012.
- [10] Jared Di Carlo, Patrick M Wensing, Benjamin Katz, Gerardo Bledt, and Sangbae Kim. Dynamic locomotion in the mit cheetah 3 through convex model-predictive control. In *2018 IEEE/RSJ international conference on intelligent robots and systems (IROS)*, pages 1–9. IEEE, 2018.
- [11] Jeffrey Duperret, Benjamin Kramer, and Daniel E Koditschek. Core actuation promotes self-manipulability on a direct-drive quadrupedal robot. In *International Symposium on Experimental Robotics*, pages 147–159. Springer, 2016.
- [12] Peter Eckert, Alexander Spröwitz, Hartmut Witte, and Auke Jan Ijspeert. Comparing the effect of different spine and leg designs for a small bounding quadruped robot. In *2015 IEEE International Conference on Robotics and Automation (ICRA)*, pages 3128–3133. IEEE, 2015.
- [13] Roy Featherstone. *Rigid body dynamics algorithms*. Springer, 2008.
- [14] Callen Fisher, Stacey Shield, and Amir Patel. The effect of spine morphology on rapid acceleration in quadruped robots. In *2017 IEEE/RSJ International Conference on Intelligent Robots and Systems (IROS)*, pages 2121–2127. IEEE, 2017.
- [15] Nicholas Hafner, Chaoran Liu, Carlos Ishi, and Hiroshi Ishiguro. Quadrupedal spine control strategies: exploring correlations between system dynamic responses and human perspectives. *Advanced Robotics*, 39(6):273–290, 2025.
- [16] Donald F Hoyt and C Richard Taylor. Gait and the energetics of locomotion in horses. *Nature*, 292(5820): 239–240, 1981.
- [17] Benjamin Katz, Jared Di Carlo, and Sangbae Kim. Mini cheetah: A platform for pushing the limits of dynamic quadruped control. In *2019 international conference on robotics and automation (ICRA)*, pages 6295–6301. IEEE, 2019.
- [18] Nathan Kau, Aaron Schultz, Natalie Ferrante, and Patrick Slade. Stanford doggo: An open-source, quasi-direct-drive quadruped. In *2019 International conference on robotics and automation (ICRA)*, pages 6309–6315. IEEE, 2019.
- [19] Mahdi Khoramshahi, Alexander Spröwitz, Alexandre Tuleu, Majid Nili Ahmadabadi, and Auke Jan Ijspeert. Benefits of an active spine supported bounding locomotion with a small compliant quadruped robot. In *2013 IEEE international conference on robotics and automation*, pages 3329–3334. IEEE, 2013.
- [20] Wanyue Li, Zida Zhou, and Hui Cheng. Dynamic locomotion of a quadruped robot with active spine via model predictive control. In *2023 IEEE International Conference on Robotics and Automation (ICRA)*, pages 1185–1191. IEEE, 2023.
- [21] Avadesh Meduri, Paarth Shah, Julian Viereck, Majid Khadiv, Ioannis Havoutis, and Ludovic Righetti. Bi-conmp: A nonlinear model predictive control framework for whole body motion planning. *IEEE Transactions on Robotics*, 39(2):905–922, 2023.
- [22] Jing Na, Qiang Chen, and Xuemei Ren. Chapter 1 - friction dynamics and modeling. In Jing Na, Qiang Chen, and Xuemei Ren, editors, *Adaptive Identification and Control of Uncertain Systems with Non-smooth Dynamics*, pages 11–18. Academic Press, 2018. ISBN 978-0-12-813683-6.
- [23] Yoshihiko Nakamura and Hideo Hanafusa. Inverse kinematic solutions with singularity robustness for robot manipulator control. 1986.
- [24] Soha Pouya, Mohammad Khodabakhsh, Alexander Spröwitz, and Auke Ijspeert. Spinal joint compliance and actuation in a simulated bounding quadruped robot. *Autonomous Robots*, 41(2):437–452, 2017.
- [25] Marc H Raibert. *Legged robots that balance*. MIT press, 1986.
- [26] Nadja Schilling and Rémi Hackert. Sagittal spine movements of small therian mammals during asymmetrical gaits. *Journal of Experimental Biology*, 209(19):3925–3939, 2006.
- [27] Theo H Smit. The use of a quadruped as an in vivo model for the study of the spine—biomechanical considerations. *European spine journal*, 11(2):137–144, 2002.
- [28] Emanuel Todorov, Tom Erez, and Yuval Tassa. Mujoco: A physics engine for model-based control. In *2012 IEEE/RSJ International Conference on Intelligent Robots and Systems*, pages 5026–5033. IEEE, 2012. doi: 10.1109/IROS.2012.6386109.

- [29] Yue Wang. bard: Batched Articulated Robot Dynamics, October 2025. URL <https://github.com/YueWang996/bard>.
- [30] Keran Ye and Konstantinos Karydis. Modeling and trajectory optimization for standing long jumping of a quadruped with a preloaded elastic prismatic spine. In *2021 IEEE/RSJ International Conference on Intelligent Robots and Systems (IROS)*, pages 902–908. IEEE, 2021.
- [31] Keran Ye, Kenneth Chung, and Konstantinos Karydis. A novel lockable spring-loaded prismatic spine to support agile quadrupedal locomotion. In *2023 IEEE/RSJ International Conference on Intelligent Robots and Systems (IROS)*, pages 2776–2783. IEEE, 2023.
- [32] Xiuli Zhang, Hongbo Yu, Boyu Liu, and Xiaoxu Gu. A bio-inspired quadruped robot with a global compliant spine. In *2013 IEEE International Conference on Robotics and Biomimetics (ROBIO)*, pages 1312–1316. IEEE, 2013.
- [33] Xiuli Zhang, Chenliang Zhao, Zhongqi Xu, and Senwei Huang. Mechanism analysis of cheetah’s high-speed locomotion based on digital reconstruction. *Biomimetic Intelligence and Robotics*, 2(1):100033, 2022.